CrossMark click for updates

Differential structured illumination microendoscopy for in vivo imaging of molecular contrast agents

Pelham Keahey[a], Preetha Ramalingam[b], Kathleen Schmeler[c], and Rebecca R. Richards-Kortum[a,1]

[a]Department of Bioengineering, Rice University, Houston, TX 77030; [b]Department of Pathology, The University of Texas MD Anderson Cancer Center, Houston, TX 77030; and [c]Department of Gynecologic Oncology and Reproductive Medicine, The University of Texas MD Anderson Cancer Center, Houston, TX 77030

This contribution is part of the special series of Inaugural Articles by members of the National Academy of Sciences elected in 2015.

Contributed by Rebecca R. Richards-Kortum, August 18, 2016 (sent for review July 1, 2016; reviewed by Marlan O. Scully and Melissa C. Skala)

Fiber optic microendoscopy has shown promise for visualization of molecular contrast agents used to study disease in vivo. However, fiber optic microendoscopes have limited optical sectioning capability, and image contrast is limited by out-of-focus light generated in highly scattering tissue. Optical sectioning techniques have been used in microendoscopes to remove out-of-focus light but reduce imaging speed or rely on bulky optical elements that prevent in vivo imaging. Here, we present differential structured illumination microendoscopy (DSIMe), a fiber optic system that can perform structured illumination in real time for optical sectioning without any opto-mechanical components attached to the distal tip of the fiber bundle. We demonstrate the use of DSIMe during in vivo fluorescence imaging in patients undergoing surgery for cervical adenocarcinoma in situ. Images acquired using DSIMe show greater contrast than standard microendoscopy, improving the ability to detect cellular atypia associated with neoplasia.

molecular imaging | cervical cancer | microendoscopy | fluorescence | structured illumination

Advances in targeted optically active contrast agents have provided new tools to image disease-related biomarkers in living tissue (1–4). When coupled with appropriate imaging systems, these molecular probes can be used to dynamically monitor molecular pathways associated with carcinogenesis, help detect precancerous lesions at an early stage, better identify tumor margins, and evaluate therapeutic response (5, 6). Optical imaging can provide the necessary spatiotemporal resolution to monitor molecular probes at the cellular level; however, imaging living tissue in vivo presents many challenges to realizing subcellular resolution.

Fiber optic microendoscopy has proven well-suited for minimally invasive high resolution imaging of hollow organs at subcellular resolution (7, 8). When used in conjunction with contrast agents, high resolution microendoscopy (HRME) has shown promise to improve early detection of precancerous lesions based on changes in nuclear size, shape, and density (9–15). However, the coherent fiber optic bundles used in microendoscopes lack inherent optical sectioning capabilities (8); out-of-focus light generated in highly scattering tissues can result in poor image contrast that obscures cellular detail (16, 17), which is particularly problematic in tissues with glandular epithelium, such as the breast, where microendoscopic images do not show sufficient contrast to differentiate between normal and neoplastic tissue (18). Similar difficulties have been noted in imaging glandular tissue of the cervix (17).

To improve image contrast, fiber optic confocal microendoscopes have been developed. Confocal sectioning typically requires inclusion of a beam-scanning system at either the proximal or distal end of the fiber bundle. Complex, miniature opto-mechanical components are required to incorporate scanning at the distal tip of the microendoscope (19–22). Alternatively, confocal scanning mechanisms can be incorporated at the proximal end of the endoscope (22–24). Proximal scanning facilitates probe miniaturization and robustness particularly when using long flexible bundles in clinical endoscopy. However, confocal raster or line-scanning mechanisms can limit image acquisition rate and require strong illumination intensities due to loss from pin-hole detector masks (8). Alternatively, structured illumination (SI) can be used to perform optical sectioning comparable in strength with confocal microscopy at reduced illumination intensities that can be achieved with lamp or LED excitation (25). SI microendoscopy improves visualization of nuclear morphology compared with standard microendoscopy (17, 26, 27). However, a major drawback of SI is the need to obtain multiple images in sequence that must be combined to produce a single sectioned image. Any motion during the acquisition of these frames produces significant image artifacts that obscure cellular detail (17). It is particularly difficult to avoid motion artifact when imaging through a handheld fiber bundle in contact with soft tissue. Additionally, any error in phase shifting the modulation during sequential acquisition can produce artifacts. To reduce motion artifacts, a digital micromirror device (DMD) can be used to produce the structured illumination pattern (27, 28); the DMD can rapidly change illumination patterns, and image frames can be acquired at sufficiently high speeds to avoid between-frame motion. However, imaging at faster frame rates comes at the expense of reduced light collection time, which presents a challenge for fluorophores with low quantum efficiency or high susceptibility to photobleaching.

Wilson suggested an alternate method of optical sectioning using SI that does not require sequential collection of three images (25). A reflective disk grating is used to modulate light in both the excitation and emission pathways. Excitation light is modulated by the grating, creating structured illumination at the

Significance

Advances in molecular-targeted optical imaging probes offer the opportunity to identify and monitor pathophysiologic processes; to achieve this promise, there is an important need to develop devices capable of imaging probes in vivo at the cellular level. The challenge is to build devices that overcome the many optical and mechanical challenges associated with imaging soft tissue inside the body. Fiber optic microendoscopy has shown promise for in vivo imaging, but image contrast in highly scattering tissue is severely limited by out-of-focus light. In this paper, we demonstrate differential structured illumination microendoscopy (DSIMe) to image molecular contrast agents in vivo. We demonstrate improved image contrast of DSIMe when imaging patients with cervical adenocarcinoma in situ to detect atypia associated with neoplasia.

Author contributions: P.K. designed research; P.K., P.R., and K.S. performed research; P.K. contributed new reagents/analytic tools; P.K., P.R., K.S., and R.R.K. analyzed data; and P.K., P.R., K.S., and R.R.K. wrote the paper.

Reviewers: M.O.S., Texas A&M University, Princeton University, and Baylor University; and M.C.S., Morgridge Institute for Research.

The authors declare no conflict of interest.

Freely available online through the PNAS open access option.

[1]To whom correspondence should be addressed. Email: rkortum@rice.edu.

Downloaded at Palestinian Territory, occupied on December 13, 2021

www.manaraa.com

focus plane. Two images of the returning emission light are recorded simultaneously: one of the light transmitted through the grating and a second of the light reflected off the grating. Each image corresponds to detector masks of complementary transmittance. Subtracting the two images yields an optically sectioned image. The grating is rotated rapidly relative to the exposure time of the image sensor to average out the modulation. Because both images are recorded simultaneously, combined sectioned images can be recorded without motion artifacts (25). Commercial laboratory microscopes (Andor and Zeiss) have been developed to record sectioned images using this principle, termed "aperture correlation" or "differential spinning disk" (29). However, these systems are not portable, are not designed for in vivo use, and are costly. To our knowledge, reflective spinning disk structured illumination has not been demonstrated in a fiber optic microendoscope.

Here, we present a differential structured illumination microendoscope (DSIMe). The DSIMe performs optical sectioning at video rate without suffering motion artifact. The system does not require any optics or scanning mechanism at the distal end of the fiber bundle, making it ideal for in vivo use. We quantified the axial response of the system using an optical phantom and show that improved optical sectioning results in improved image contrast in an ex vivo animal model. A clinical pilot study was then performed to demonstrate in vivo imaging in patients undergoing surgical treatment with conization for cervical adenocarcinoma in situ (AIS). Results demonstrate contrast enhancement and improved ability to detect the cellular atypia associated with neoplasia in real time.

Results and Discussion

The DSIMe system is designed to offer a portable platform to perform in vivo imaging in an operating room or clinic setting. The optical layout and a photograph of the DSIMe system are shown in Fig. 1. A high power LED provides illumination, and a spinning reflective grating modulates the illumination pathway, which is imaged onto a coherent fiber optic bundle placed in contact with the tissue surface. Modulated excitation light is relayed to the sample by the fiber bundle; corresponding modulated emission light returns via the same optical path and is imaged onto the reflective disk grating via the objective and relay lens. Light emanating from in-focus and out-of-focus optical planes of the fiber bundle passes through the grating unobstructed and is imaged by a tube lens onto the rear CCD, resulting in a widefield image. Light from optical planes past the point where the grating image on the fiber bundle has decayed due to defocus strikes the reflective grating and is reflected toward a second optical pathway; this out-of-focus background light is imaged onto the front CCD. The rate of decay due to defocus in SI imaging depends on the grating modulation frequency (25). The grating is rotated rapidly relative to the exposure time of the CCD to average out the modulation in both images. Proper spatial coregistration is maintained through the use of a real-time image stabilization algorithm. Images can be displayed via computer monitor or wirelessly relayed to a pair of smart glasses (Fig. 1 *B* and *C*). The smart glass interface is used to relay images directly to clinicians during in vivo operation of the device. This feature allows clinicians using the DSIMe to simultaneously watch where they are placing the fiber bundle during imaging and see images and instrument status.

To demonstrate the performance of axial sectioning using the DSIMe, fluorescent 15-μm microspheres (Life Technologies) were deposited onto a clear glass microscope slide. After the microspheres were deposited onto the glass slide, the slide was placed in contact and slowly stepped away from the fiber bundle. Fig. 2 shows images of the fluorescent microspheres at different distances from the distal tip of the fiber bundle. In widefield (Fig. 2 *A*–*C*) images, microspheres are clearly visible at distances up to 100 μm, with increased size due to defocus. In contrast, DSIMe images show improved optical sectioning as the frequency of modulation is increased. Using a grating with 9 lines per millimeter (lpm), microspheres were no longer visible at a distance of 100 μm (Fig. 2 *D*–*F*). At 25 lpm, microspheres in DSIMe images (Fig. 2 *G*–*I*) were no longer visible at a distance of 50 μm. Average sphere intensity vs. distance is quantified in Fig. 2*J*. Without SI, the average intensity changed minimally with increasing distance between the sample and the distal tip of the fiber bundle. With SI, the intensity attenuated more rapidly as the distance between the sample and the distal tip of the fiber bundle increases, illustrating

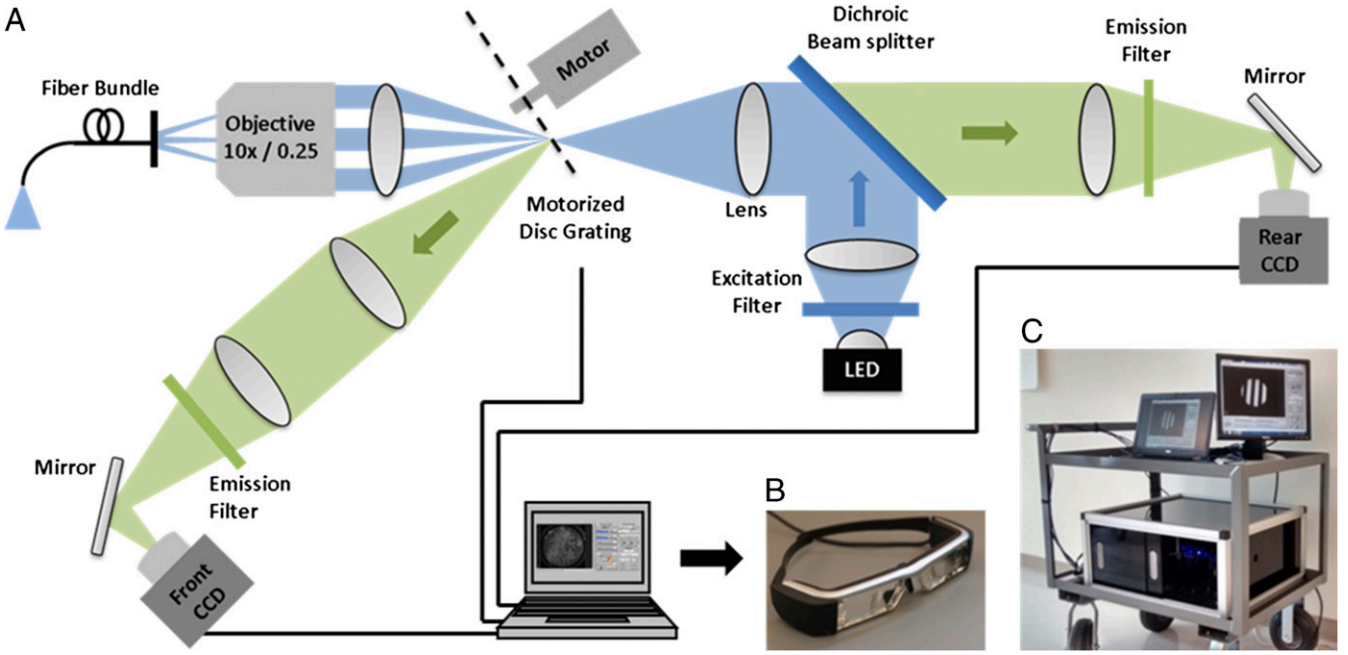

Fig. 1. (*A*) Optical layout of the DSIMe system. (*B*) Photograph of the smart glass system used with the DSIMe system to send visual and device information to clinicians during in vivo operation. (*C*) Photograph of the portable DSIMe optical enclosure and computer system for moving to the clinic and operating room.

Downloaded at Palestinian Territory, occupied on December 13, 2021
www.manaraa.com

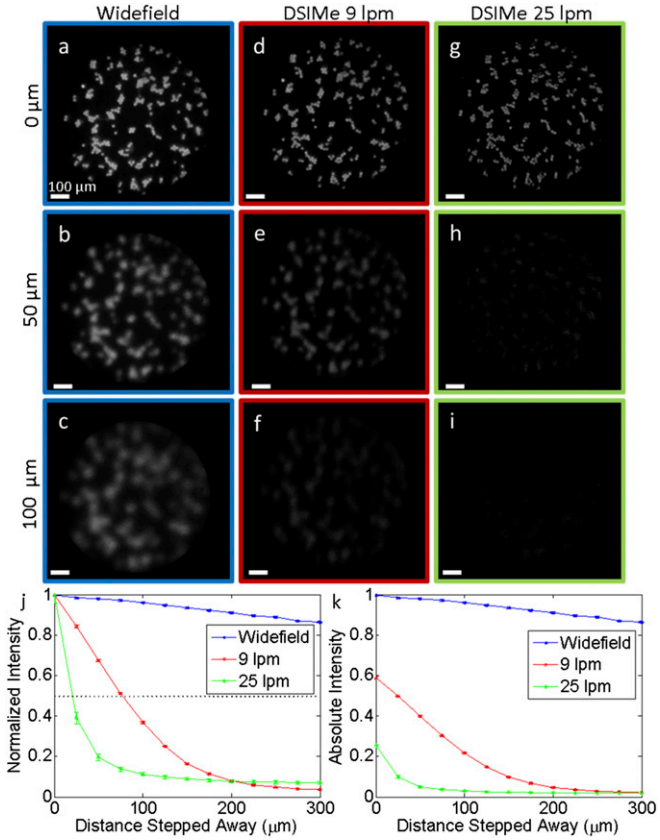

Fig. 2. (*A–C*) Widefield images of microspheres at different distances from the distal tip of the fiber bundle. (*D–F*) DSIMe images at 9 lpm modulation frequency of microspheres. (*G–I*) DSIMe images at 25 lpm modulation frequency. Quantified sphere intensity normalized (*J*) and absolute (*K*) vs. distance from the tip of the fiber bundle to the sample at each modulation frequency. Brightness is adjusted equally for all images.

the optical sectioning capability of DSIMe. Microsphere intensity at 9 lpm reached 50% initial intensity at ~75 µm. At 25 lpm, microsphere intensity reached 50% initial intensity at sub-25 µm. Measuring microsphere intensity attenuation with respect to distance demonstrated a modulation frequency dependence on axial sectioning strength. However, as shown in Fig. 2*K*, more in-focus light was lost at higher modulation frequencies. In-focus signal attenuation was ~40% at 9 lpm and 75% for 25 lpm, illustrating the trade-offs between sectioning and signal. Increasing the modulation frequency to increase sectioning strength came at the expense of signal loss at higher modulation frequencies, which has been observed in previous work using SI in microendoscopes (17, 27).

To determine whether the improved axial sectioning capabilities of DSIMe observed with the microsphere phantom in air would translate to contrast enhancement in highly scattering tissue, excised mouse tissue was imaged ex vivo. Proflavine [0.01% (wt/vol) in sterile PBS], a fluorescent contrast agent that stains cell nuclei, was topically applied to mouse stomach and colon to highlight nuclei found in glandular walls. Images were acquired immediately after application (30). Fig. 3 shows representative widefield and DSIMe images of excised mouse tissue. Use of DSIMe visibly improved contrast in images of mouse colon (Fig. 3 *A* and *B*) and stomach (Fig. 3 *C* and *D*). DSIMe signal from the line scans in Fig. 3 *E* and *F* show improved contrast between glandular wall and lumen compared with widefield images. To quantify the improvement in image contrast, the average normalized intensity for the gland walls (maxima) was compared with the average intensity of the lumen (minima) indicated by the brackets in Fig. 3 *E* and *F*. The average intensity of maxima and minima were compared for images of nine colon and 14 stomach sites in the same manner. The ratio of the average maxima to minima was 28 ± 7% higher in DSIMe images of colon tissue than in widefield images (1.21 ± 0.06 for widefield to 1.56 ± 0.17 for DSIMe, $P < 0.0001$). Similarly, contrast was 48 ± 20% higher in DSIMe images of stomach than in widefield (1.78 ± 0.22 for widefield to 2.61 ± 0.35 for DSIMe, $P < 0.0001$).

To demonstrate clinical utility of the DSIMe device, cervical tissue was imaged in vivo in patients undergoing surgical treatment with conization for AIS. Before imaging, proflavine was topically applied to the cervix. The fiber bundle probe tip was placed in contact with visually normal and abnormal areas, and widefield and DSIMe images were obtained by the clinician. All images were displayed in real-time via computer monitor or smart glass system. Fig. 4 shows representative widefield and DSIMe images of normal and neoplastic tissue. Fig. 4 *A–E* shows widefield and DSIMe images and corresponding histology of a region of normal squamous epithelium at the boundary of high grade squamous intraepithelial lesion (HSIL). Normal squamous epithelium is characterized by regularly spaced, small nuclei. In contrast, the area of HSIL showed larger, more closely spaced nuclei, which is consistent with previous studies using high resolution microendoscopy to study squamous epithelium where increased nuclear density and nuclear size are observed and can be quantified in dysplastic tissue (13, 14, 31). The DSIMe images corresponding to the HSIL region showed improved image contrast. Images shown in Fig. 4 *F–J* show an area of HSIL characterized by increased nuclear size, density, and pleomorphism compared with the normal squamous epithelium shown in Fig. 4 *A* and *B*. Again, contrast enhancement was observed in the DSIMe image, facilitating visualization of nuclear morphometry. Fig. 4 *K–O* is from a region of tissue containing HSIL with underlying adenocarcinoma. Contrast is improved in the DSIMe image, facilitating imaging of epithelial cell nuclei.

Conclusions

Here, we demonstrate a high resolution fiber optic microendoscope capable of performing real-time differential structured illumination in vivo without motion artifacts. All of the optical components are located on the proximal side of the fiber bundle, which better facilitates small probes for in vivo imaging. It is conceivable that

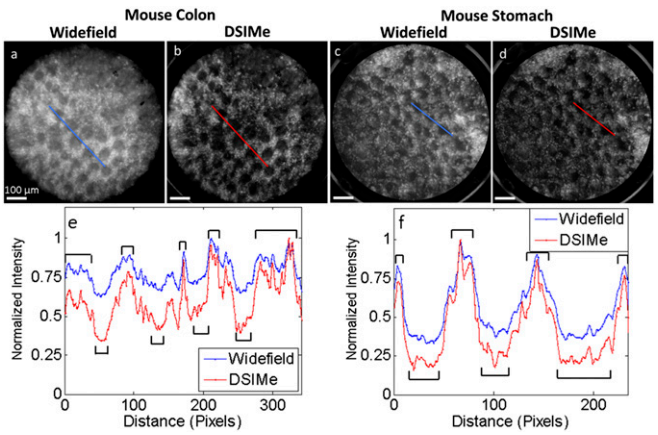

Fig. 3. (*A*) Widefield image of mouse colon compared with (*B*) DSIMe image of the same site. (*C*) Widefield image of mouse stomach compared with (*D*) DSIMe image of the same site. Line scans of mouse (*E*) colon and (*F*) stomach comparing widefield and DSIMe images. Brightness and contrast were adjusted equally for visual comparison after quantification using line scans. Images shown are what the device displayed in real time to the user without fiber core removal.

Downloaded at Palestinian Territory, occupied on December 13, 2021
www.manaraa.com

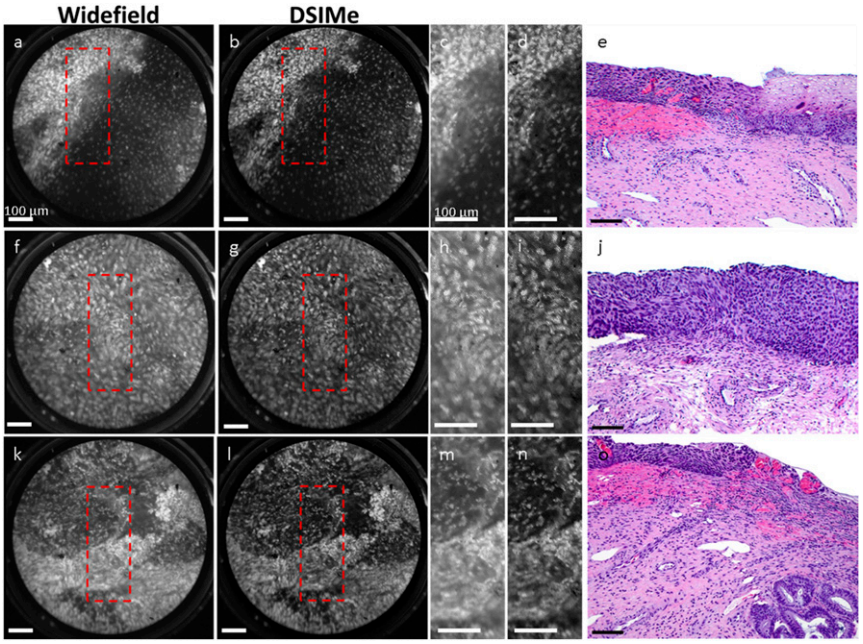

Fig. 4. (*A*) Widefield and (*B*) DSIMe images of tissue at the boundary between normal squamous epithelium and a high grade squamous intraepithelial lesion (HSIL). The DSIMe image shows improved contrast compared with the widefield image. Contrast enhancement is more readily observed in the zoomed-in regions indicated by the dashed box (*C* and *D*). Pathology (*E*) from this region revealed a boundary between HSIL and normal squamous epithelium. Widefield (*F*) and DSIMe (*G*) show an area of tissue with increased nuclear size and density compared with normal squamous epithelium. Increased contrast in DSIMe images can be seen in the zoomed-in regions (*H* and *I*). Pathology (*J*) from this region showed HSIL. Widefield (*K*) and DSIMe (*L*) show an image from a region of tissue containing HSIL with underlying adenocarcinoma. Contrast is improved in DSIMe images compared with widefield and in zoomed-in areas (*M* and *N*). Pathology (*O*) from this region of tissue found areas of HSIL and adenocarcinoma. (Scale bars: 100 μm.)

DSIMe could be used in conjunction with fiber bundles that have additional optics attached at the distal tip to further improve spatial resolution and provide subsurface imaging (26, 27) although this idea must be further evaluated.

As demonstrated in the optical phantom, sectioning strength varies with modulation frequency. Increasing the modulation frequency to increase sectioning strength comes at the expense of signal loss at higher modulation frequencies, which has been discussed in previous work using SI in microendoscopes (17, 27). Despite this loss, DSIMe images of scattering mouse and human tissue show higher image contrast in comparison with widefield microendoscopy. Improvements in image contrast enable improved recognition of nuclear morphometry, particularly in areas of precancer and cancer. Although visually compelling, the improved nuclear recognition could also improve automated algorithms designed to identify neoplasia in real time that would otherwise struggle in highly scattering tissue (14, 32, 33). Additionally, because DSIMe maintains the small size of the probe, this technique could be used to improve high resolution microendoscopy imaging in a wider array of tissues. Other studies using high resolution microendoscopy have been conducted to study esophageal (34), liver and pancreas (9), colon (30), and oral (12) cancers. The fiber probe is small enough to fit into the biopsy channel of a standard endoscope, allowing it to be used in conjunction with current endoscopy. Differential structured illumination microendoscopy offers a promising technique to improve image contrast in real time without motion artifacts or the need to sacrifice miniaturization of the probe, which better facilitates in vivo imaging of tissue in conjunction with molecular contrast agents.

Materials and Methods

DSIMe Optical Layout and Operation. Fig. 1*A* shows the optical layout of the DSIMe system. A high power LED (M455L3; Thorlabs) emits 455-nm light, which passes through an excitation filter (ET470/40×; Chroma) and is collimated by a collection lens. The excitation light passes through a relay lens, reflects off a dichroic beamsplitter (475DCXRU; Chroma), and illuminates the custom disk grating (Applied Image). The grating rotates continuously at 110 rpm (T-NM; Zaber) during imaging to average out the grating pattern in the final images. The modulated excitation light is imaged via a second relay lens onto the rear of the objective (RMS10X; Olympus). A fiber optic bundle (Myriad Fiber Imaging) comprising 30,000 individual fibers is placed at the objective's working distance. Modulated excitation light is relayed to the sample by the fiber bundle. Corresponding modulated emission light returns via the same path. The returning modulated fluorescence emission is imaged onto the reflective disk grating via the objective and the same relay lens. Light emanating from in-focus and out-of-focus optical planes of the fiber bundle passes through the grating unobstructed and is imaged by a tube lens onto the rear CCD, resulting in a widefield image. Light from optical planes past the defocus point of the grating strikes the reflective grating and is reflected toward a second optical pathway; this out-of-focus background light is imaged onto the front CCD. The depth of the defocus point in SI imaging depends on the grating modulation frequency (25). Both CCDs are triggered simultaneously to acquire the widefield and background images. Subtracting the background image (front CCD) from the widefield image (rear CCD) yields an optically sectioned image. A multiplier is applied to the background image to account for differences in throughput between the front and rear optical pathways. The widefield image can be compared with the subtracted sectioned image for immediate comparison between standard widefield high resolution microendoscopy and DSIMe. The lateral resolution of the system is ~4.4 μm as determined by imaging an Air Force resolution target and resolving group 6 element 6. Lateral resolution is limited by the fiber bundle core size and is consistent with previously published high resolution microendoscope systems built by our laboratory using the same bundle (17).

For subtraction of the widefield and background images to accurately remove out-of-focus light, it is necessary to maintain proper spatial image coregistration between the two images. Building a motorized rotating disk grating that can remain steady at the micrometer scale is challenging and would require expensive and precisely machined components. As a low-cost, practical alternative, we developed an image stabilization routine to properly coregister the two images in real time. A one-time calibration routine during system start-up rotates the disk through one revolution in incremental steps. At each angular position of the grating, the location of the image of the fiber optic bundle is identified on the front CCD. A look-up table is then constructed correlating the angular position of the grating to the location of the fiber bundle image. During DSIMe operation, the control software records

Downloaded at Palestinian Territory, occupied on December 13, 2021
www.manaraa.com

the angular position of the grating when triggering image acquisition. Using the look-up table, an algorithm registers the images, correcting for *xy*-displacement of the fiber bundle caused by any periodic motion in the rotating disk before image subtraction. Correction occurs in real time, and the system can acquire sectioned images at frame rates up to 12 fps depending on exposure time. Images can be displayed via computer monitor or wirelessly relayed to a pair of smart glasses (Moverio; Epson) (Fig. 1 *B* and *C*). The smart glass interface is used to relay images directly to clinicians during in vivo operation of the device.

Optical Phantom. A solution containing 15-μm-diameter fluorescent polystyrene microspheres (F-21010; Life Technologies) was pipetted onto a clear glass slide; the solution was allowed to dry as described in ref. 16. The fiber bundle was placed in contact with the surface of the slide, and a first image was acquired; the slide was incrementally stepped away from the distal tip of the fiber bundle. This process was performed three times: once for widefield imaging with the reflective disk removed, and then with two discs with different grating frequencies of 9 lpm and 25 lpm. LED power was increased when the disk was removed so the average intensity at the start of each measurement was equal and exposure time of the CCDs was fixed at 15 ms. The disk was removed for widefield imaging so a comparison could be made between standard epifluorescent microendoscopy and DSIMe. Ten images were acquired at each position, and the average in intensity for each image was measured and analyzed using ImageJ (ver 1.47v; NIH) to create the graphs in Fig. 2. Bead intensity for Fig. 2*J* was normalized to the initial intensity measured at the 0 position for each set of images. Bead intensity for Fig. 2*K* was normalized to the 0 position of the widefield images.

Ex Vivo Mouse Tissue Imaging. Mouse tissue was obtained from female C57/BL6J mice 12 to 16 wk of age. All mouse experiments were performed in accordance with an institutional animal care and use committee-approved protocol at Rice University. Proflavine [0.01% (wt/vol) in sterile PBS], a fluorescent contrast agent that stains cell nuclei, was topically applied to excised mouse stomach and colon and imaged immediately with DSIMe. Imaging was performed with the 9-lpm disk grating, and exposure time of the CCDs was 40 ms and gain was adjusted from 0 to 10 dB to minimize pixel saturation. The fiber optic bundle was placed in gentle contact with the mucosa and scanned across the tissue surface. To compare signal and background intensity in DSIMe and widefield images, line scans were plotted across the same location in widefield and DSIMe images in images of mouse tissue. To remove the fixed pattern associated with the fiber bundle, a fiber core removal algorithm was used (35). In brief, the algorithm interpolates the pixel intensity of the fiber cladding based on the pixel intensities within the fiber core. The intensity value of the center pixel is then used to assign all noncenter pixels the same intensity value to the nearest center pixel, giving the cladding the same pixel intensity as the core. Core removal and line scans were performed on raw widefield and DSIMe images before any contrast or brightness adjustments. The core removal algorithm and line scans were performed in postprocessing using a Matlab script and ImageJ, respectively.

In Vivo Cervical Tissue Imaging. The optical performance of the DSIMe system using a reflective grating of 9 lpm was evaluated in an institutional review board (IRB)-approved pilot study of patients undergoing cold knife cone (CKC) treatment for diagnosed AIS. Patients gave informed consent, and the study was reviewed and approved by the IRBs at Rice University and University of Texas MD Anderson Cancer Center. Five patients out of 20 total enrollment were imaged. Results presented in Fig. 4 are from one patient and are representative of our results. Before imaging, proflavine hemisulfate [0.01% (wt/vol) in sterile PBS] and Lugol's iodine were topically applied to the cervix. After application of proflavine, the DSIMe probe was advanced through the speculum and used to image the cervix. Images were acquired of areas of colposcopically normal and abnormal areas of the cervix. Exposure time of the CCDs was 40 ms, and gain was adjusted from 0 to 10 dB to minimize pixel saturation. Clock positions of the images were noted at the time of imaging. After surgical excision, the cervical cone specimen was submitted for routine pathology review by a board-certified gynecologic pathologist. Images of stained sections were acquired from regions of tissue imaged with the DSIMe.

ACKNOWLEDGMENTS. We thank the clinical research support staff at MD Anderson for their tireless work and effort in supporting this work. Research reported in this publication was supported by National Cancer Institute, National Institutes of Health Grants R01CA140257, R01CA103830, and R01CA186132. The content is solely the responsibility of the authors and does not necessarily represent the official views of the National Institutes of Health.

1. Pierce MC, Javier DJ, Richards-Kortum R (2008) Optical contrast agents and imaging systems for detection and diagnosis of cancer. *Int J Cancer* 123(9):1979–1990.
2. Geva-Zatorsky N, et al. (2015) In vivo imaging and tracking of host-microbiota interactions via metabolic labeling of gut anaerobic bacteria. *Nat Med* 21(9):1091–1100.
3. Wu SC, et al. (2016) Bispecific antibody conjugated manganese-based magnetic engineered iron oxide for imaging of HER2/neu- and EGFR-expressing tumors. *Theranostics* 6(1):118–130.
4. Carns J, Keahey P, Quang T, Anandasabapathy S, Richards-Kortum R (2013) Optical molecular imaging in the *gastrointestinal tract. Gastrointest Endosc Clin N Am* 23(3): 707–723.
5. Freise AC, Wu AM (2015) In vivo imaging with antibodies and engineered fragments. *Mol Immunol* 67(2 Pt A):142–152.
6. Brindle K (2008) New approaches for imaging tumour responses to treatment. *Nat Rev Cancer* 8(2):94–107.
7. Gu M, Bao H, Kang H (2014) Fibre-optical microendoscopy. *J Microsc* 254(1):13–18.
8. Flusberg BA, et al. (2005) Fiber-optic fluorescence imaging. *Nat Methods* 2(12):941–950.
9. Regunathan R, et al. (2012) Feasibility and preliminary accuracy of high-resolution imaging of the liver and pancreas using FNA compatible microendoscopy (with video). *Gastrointest Endosc* 76(2):293–300.
10. Pierce M, Yu D, Richards-Kortum R (2011) High-resolution fiber-optic microendoscopy for in situ cellular imaging. *J Vis Exp* 2011(47):2306.
11. Parikh ND, et al. (2014) In vivo diagnostic accuracy of high-resolution microendoscopy in differentiating neoplastic from non-neoplastic colorectal polyps: A prospective study. *Am J Gastroenterol* 109(1):68–75.
12. Muldoon TJ, et al. (2012) Noninvasive imaging of oral neoplasia with a high-resolution fiber-optic microendoscope. *Head Neck* 34(3):305–312.
13. Pierce MC, et al. (2012) Accuracy of in vivo multimodal optical imaging for detection of oral neoplasia. *Cancer Prev Res (Phila)* 5(6):801–809.
14. Quinn MK, et al. (2012) High-resolution microendoscopy for the detection of cervical neoplasia in low-resource settings. *PLoS One* 7(9):e44924.
15. Muldoon TJ, et al. (2007) Subcellular-resolution molecular imaging within living tissue by fiber microendoscopy. *Opt Express* 15(25):16413–16423.
16. Koucky MH, Pierce MC (2013) Axial response of high-resolution microendoscopy in scattering media. *Biomed Opt Express* 4(10):2247–2256.
17. Keahey PA, Tkaczyk TS, Schmeler KM, Richards-Kortum RR (2015) Optimizing modulation frequency for structured illumination in a fiber-optic microendoscope to image nuclear morphometry in columnar epithelium. *Biomed Opt Express* 6(3):870–880.
18. Dobbs J, et al. (2016) High resolution microendoscopy with structured illumination and Lugol's iodine staining for evaluation of breast cancer architecture. *Proc SPIE* 9703:97030E–97030E–11.
19. Ducourthial G, et al. (2015) Development of a real-time flexible multiphoton microendoscope for label-free imaging in a live animal. *Sci Rep* 5:18303.
20. Piyawattanametha W, et al. (2012) In vivo near-infrared dual-axis confocal microendoscopy in the human lower gastrointestinal tract. *J Biomed Opt* 17(2):021102.
21. Pillai RS, Lorenser D, Sampson DD (2011) Deep-tissue access with confocal fluorescence microendoscopy through hypodermic needles. *Opt Express* 19(8):7213–7221.
22. Rouse AR, Gmitro AF (2000) Multispectral imaging with a confocal microendoscope. *Opt Lett* 25(23):1708–1710.
23. Carlson K, et al. (2005) In vivo fiber-optic confocal reflectance microscope with an injection-molded plastic miniature objective lens. *Appl Opt* 44(10):1792–1797.
24. Liang C, Sung KB, Richards-Kortum RR, Descour MR (2002) Design of a high-numerical-aperture miniature microscope objective for an endoscopic fiber confocal reflectance microscope. *Appl Opt* 41(22):4603–4610.
25. Wilson T (2011) Optical sectioning in fluorescence microscopy. *J Microsc* 242(2): 111–116.
26. Kyrish M, et al. (2013) Needle-based fluorescence endomicroscopy via structured illumination with a plastic, achromatic objective. *J Biomed Opt* 18(9):096003.
27. Bozinovic N, Ventalon C, Ford T, Mertz J (2008) Fluorescence endomicroscopy with structured illumination. *Opt Express* 16(11):8016–8025.
28. Xu D, et al. (2013) Fast optical sectioning obtained by structured illumination microscopy using a digital mirror device. *J Biomed Opt* 18(6):060503.
29. Wilson T, Juskaitis R, Neil MA, Kozubek M (1996) Confocal microscopy by aperture correlation. *Opt Lett* 21(23):1879–1981.
30. Chang SS, et al. (2013) High resolution microendoscopy for classification of colorectal polyps. *Endoscopy* 45(7):553–559.
31. Quang T, et al. (March 30, 2016) A tablet-interfaced high-resolution microendoscope with automated image interpretation for real-time evaluation of esophageal squamous cell neoplasia. *Gastrointest Endosc*, 10.1016/j.gie.2016.03.1472.
32. Shin D, et al. (2015) Quantitative analysis of high-resolution microendoscopic images for diagnosis of esophageal squamous cell carcinoma. *Clin Gastroenterol Hepatol* 13(2):272–279.e2.
33. Ishijima A, et al. (2015) Automated frame selection process for high-resolution microendoscopy. *J Biomed Opt* 20(4):46014.
34. Louie JS, Shukla R, Richards-Kortum R, Anandasabapathy S (2015) High-resolution microendoscopy in differentiating neoplastic from non-neoplastic colorectal polyps. *Best Pract Res Clin Gastroenterol* 29(4):663–673.
35. Bedard N, Quang T, Schmeler K, Richards-Kortum R, Tkaczyk TS (2012) Real-time video mosaicing with a high-resolution microendoscope. *Biomed Opt Express* 3(10): 2428–2435.

INAUGURAL ARTICLE
MEDICAL SCIENCES
Downloaded at Palestinian Territory, occupied on December 13, 2021
www.manaraa.com